IEEE Access
Multidisciplinary | Rapid Review | Open Access Journal

Received 5 April 2024, accepted 25 May 2024, date of publication 1 July 2024, date of current version 9 July 2024.

Digital Object Identifier 10.1109/ACCESS.2024.3421317

RESEARCH ARTICLE

Modulated Predictive Current Control of Photovoltaic Central NPC Inverter With Reduced Computational Burden

ALEXANDER DAHLMANN, (Member, IEEE), AND VENKATA YARAMASU, (Senior Member, IEEE)
School of Informatics, Computing and Cyber Systems, Northern Arizona University, Flagstaff, AZ 86011, USA
Corresponding author: Alexander Dahlmann (ad953@nau.edu)

ABSTRACT This paper proposes a computationally efficient modulated model predictive current control method for a three-phase neutral-point clamped (NPC) central inverter in the photovoltaic energy system. The proposed control method produces optimal triangular region consisting of optimal voltage vectors through an optimization function analysis. The optimal voltage vectors along with their duty cycles are used in the modulation stage to accomplish constant switching frequency operation, low steady-state errors and fast transient response. The control method accomplishes the system requirements such as the maximum power point tracking, balancing of the DC-link capacitor voltages, grid reactive power control, and grid synchronization. The proposed method is evaluated with a MATLAB/Simulink simulation on an 817 kW system under steady-state and varying solar irradiance conditions. The experimental validation is accomplished with a dSPACE MicroLabBox for a 5 kW system to validate the simulation results.

INDEX TERMS Current control, DC/AC power conversion, digital control, multilevel inverter, photovoltaic systems, predictive control, renewable energy sources.

I. INTRODUCTION

The prominence of photovoltaic energy systems (PVES) in the current power electrical grid has recently been accelerated due to the rapid reduction of cost of PV modules and increased government subsidies favoring PV development [1]. This increase in PV demand means that the usage of photovoltaic energy systems needs to be improved and more efficient for the maximum utilization of the PV infrastructure [2]. Among the possible configurations of PVES, the usage of a central inverter topology is favored for utility-scale PVES due to the ease of implementation from the single-stage DC/AC power inverter conversion stage. Another way to improve the efficiency and reduce the cost of the system is to use a multilevel inverter, such as the three-level neutral point clamped (3L-NPC) inverter. The multilevel inverter provides benefits such as the multilevel waveform, lower requirements for the harmonic filter, and lower electromagnetic interference [1]. The central NPC inverter performs maximum power point tracking (MPPT) for active power control, in addition to grid reactive power control, grid synchronization and neutral-point voltage control.

Current control techniques used in PV industry focus on the voltage-oriented control (VOC) utilizing proportional-integral (PI) controllers and space vector modulation (SVM) in inner control loop. This control method provides low steady-state errors while producing a constant switching frequency that can be easily filtered with a grid harmonic filter [3]. The drawback to the VOC control is that the low switching frequency operation leads to sluggish transient response, making them less than ideal for high-power PVES with varying environmental conditions. Another well studied control method for the central inverter PVES is the finite control-set model predictive control (MPC) method. The MPC method solved the problems posed by the VOC method,

The associate editor coordinating the review of this manuscript and approving it for publication was Mohsin Jamil.

such as having a fast transient response, in addition to allowing for a multi-variable control, easy inclusion of system nonlinearities and robustness against the system parameter variations [4], [5], [6]. The classical MPC for a 3L-NPC inverter in PVES has been studied in [7]. A drawback to the MPC method is the lack of a modulation stage, causing a variable switching frequency that can be difficult to filter, causing high steady-state errors [8]. By including a modulation stage to the MPC method, a different control method called modulated model predictive current control (M^2PCC) can be achieved and can combine the benefits of both VOC and MPC methods while mitigating the associated negatives [9]. Including the modulation stage to the predictive model allows for the M^2PCC method to achieve a constant switching frequency, preserving the benefits from the VOC control; the predictive model allows for a better transient analysis, preserving the benefit of the MPC method. The M^2PCC method uses an optimal triangular region and produces a symmetrical switching sequence based on the voltage vectors and corresponding duty cycles, causing a constant switching frequency operation [9]. The M^2PCC method has been studied for an NPC inverter in [10], [11], and [12]. A major drawback to the M^2PCC is the high computational burden, requiring a total of 972 calculations for 36 possible triangular regions and 27 possible voltage vectors, making commercial viability limited with the NPC inverter in PVES.

Methods to reduce the computational burden have received recent attention in the literature with the primary concept being to reduce the number of voltage vectors needing to be calculated [11]. The primary approach to reducing the voltage vector selection is to limit the search to different shaped regions in the space vector diagram such as the vector shifting method discussed in [13] that define the optimal hexagonal region for the NPC inverter. The optimal hexagonal region method identifies the approximate area of the optimal vector within the space vector diagram and centers the calculations around that point. Another method is to study the optimal sector of the space vector diagram and limit the search to that area, as done in [14]. Work done in [15] highlight the usage of optimal hexagonal regions and optimal sector in NPC converter for a wind power system with MPC. Another method is the voltage window method shown in [16] for PVES where the previous voltage vector is stored, and the next voltage vector search only allows a single variable change. With the recent attention to the M^2PCC method, there have been some works on reducing the computational burden of M^2PCC method. Works in [17] and [18] have accomplished this task for current source rectifier and two-level voltage source inverter, respectively. Currently, there are no works done in applying M^2PCC method for an NPC inverter in a PVES, where the system performance changes rapidly due to the varying temperature and irradiance. Also, there are no works in reducing the computational burden for M^2PCC method for a 3L-NPC inverter.

The current gap in the literature motivated us to pursue this work. **The unique contribution of this paper is the computationally efficient M^2PCC method for PVES. This paper proposes a way to reduce the computational burden using an optimal sector approach to reduce the number of triangular regions explored in the M^2PCC method.** The proposed method is simple and reduces the computational burden from 972 calculations (36 triangular regions times 27 voltage vectors) by 95% to 48 calculations (6 triangular regions times 8 voltage vectors) without reducing the system performance or sacrificing any of the control objectives. This improves on the existing M^2PCC methods for an NPC inverter in [10], [11], and [12] by reducing the computational burden and increasing the commercial viability of M^2PCC in utility-scale PVES, while maintaining the benefits of VOC and MPC methods. The proposed control method is verified through MATLAB simulations during transient and steady-state conditions using an 817 kW PV system. A fast Fourier transform (FFT) analysis preformed for better comparisons between the proposed M^2PCC, classical M^2PCC, and classical predictive current control (PCC) methods.

The proposed method with simulation results was previously analyzed by authors in [19]. However, this paper expands on the previous paper by incorporating the grid voltage THD into the MATLAB simulations to emulate real-world grid. Moreover, experimental validation is accomplished with a dSPACE MicroLabBox on a scale-down 5 kW PV system to validate the simulation results and proposed control method. Moreover, additional models are provided for the prediction of control variables at $(k+2)$ instant to account for real time delays.

The major contributions of this work are summarized as follows:

- A computationally efficient M^2PCC method is proposed for the PVES.
- The proposed method reduces the computational burden by roughly 95%, increasing the commercial viability of the M^2PCC method.
- The proposed control scheme is validated through simulation and experimental results under the steady-state and transient conditions.

II. PROPOSED M^2PCC METHOD

The block diagram of proposed computationally efficient M^2PCC method for the 3L-NPC inverter based PVES is shown in Fig. 1. To compensate for real time delays a prediction plus prediction algorithm is used to predict behavior of system at the $(k+2)$ instant [20].

A. MEASUREMENTS

For proper implementation of the M^2PCC algorithm, measurements of the PV array voltage and current (v_{dc}, i_{pv}), the DC-link capacitor voltages (v_{C1}, v_{C2}), the grid currents (i_{ag}, i_{bg}, i_{cg}) and the grid voltages (v_{ag}, v_{bg}, v_{cg}) are required. Calculations are accomplished in the stationary

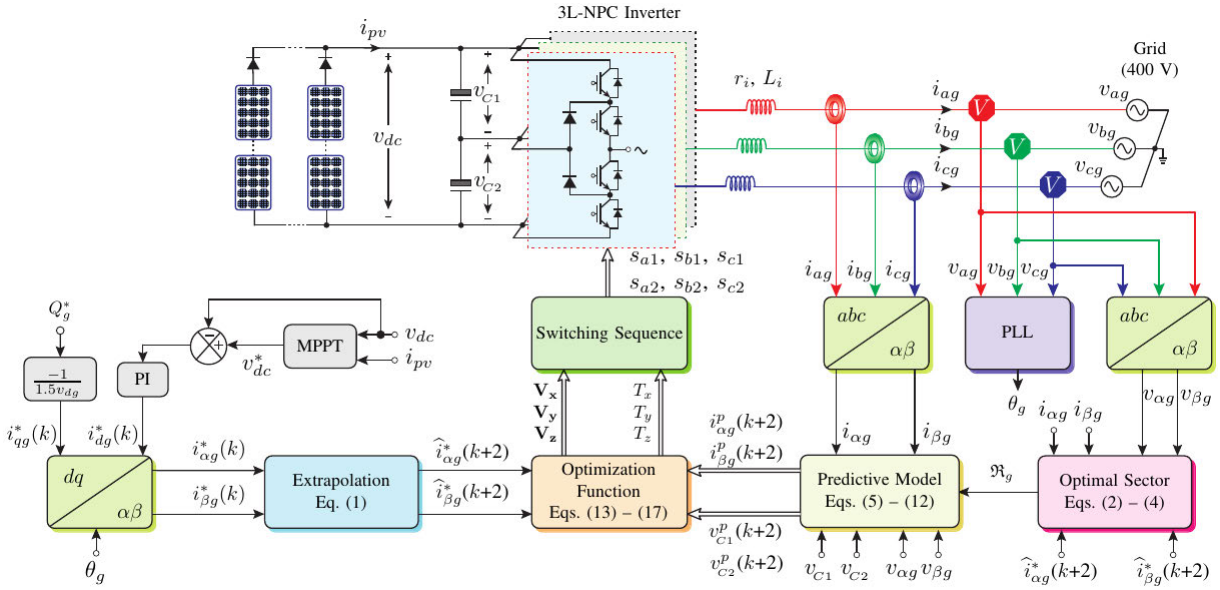

FIGURE 1. Block diagram of the proposed computationally efficient M^{2}PCC method for a 3L-NPC inverter in PVES.

($\alpha\beta$)-frame to simplify the system controls. A phase-locked loop (PLL) calculates the grid voltage angle (θ_g) for the conversions between ($\alpha\beta$)-frame and (abc)-frame and vice versa [21]. In the case of an unbalanced situation on the grid side, modifications can be made to the reference currents generation and PLL to compensate for the new disturbances [22], [23]. The inner current control loop which is presented in this paper still works well during the unbalanced grid conditions.

B. MPPT CONTROL

A perturb & observe (P&O) MPPT algorithm is applied with the PV array voltage and current (v_{dc} and i_{pv}) to produce the reference DC voltage (v^*_{dc}) at the maximum power point (MPP) [24]. The difference between the calculated reference DC voltage and measured DC-link voltage is sent to a PI controller to produce the reference d-axis grid current i^*_{dg}. The reactive power control loop provides a reference q-axis grid current i^*_{qg}. The reference dq-axis grid currents are transformed to $\alpha\beta$-axis with the help of grid voltage angle θ_g. The reference grid currents are extrapolated for the $(k+2)$ sampling instant with the help of a first order Lagrange extrapolation [20]:

$$\left.\begin{aligned}\widehat{i}^*_{\alpha g}(k+2) &= 3\,i^*_{\alpha g}(k) - 2\,i^*_{\alpha g}(k-1),\\ \widehat{i}^*_{\beta g}(k+2) &= 3\,i^*_{\beta g}(k) - 2\,i^*_{\beta g}(k-1).\end{aligned}\right\} \tag{1}$$

C. NEAREST SECTOR CALCULATION

Classical M^{2}PCC method for an NPC inverter in [10], [11], and [12] requires a total of 972 calculations for 36 possible triangular regions and 27 possible voltage vectors. The proposed optimized M^{2}PCC method evaluates 8 voltage vectors (excluding two redundant zero vectors) and 6 triangular regions in the optimal sector defined from θ_{op} and reduces the total number of calculations to 48 (8 voltage vectors times 6 triangular regions). These reduced number of calculations translate to drop in computational burden by roughly 95% (1)-$\frac{48}{972}$). The angle of reference voltage vector, θ_{op} is determined as shown below:

$$\begin{bmatrix} v^*_{\alpha i}(k) \\ v^*_{\beta i}(k) \end{bmatrix} = \frac{1}{\Gamma}\left\{\begin{bmatrix} \widehat{i}^*_{\alpha g}(k+1) \\ \widehat{i}^*_{\beta g}(k+1) \end{bmatrix} - \Phi \begin{bmatrix} i_{\alpha g}(k) \\ i_{\beta g}(k) \end{bmatrix} + \Gamma \begin{bmatrix} v_{\alpha g}(k) \\ v_{\beta g}(k) \end{bmatrix}\right\} \tag{2}$$

with,

$$\Phi = e^{-\frac{r_i T_s}{L_i}}, \quad \Gamma = \frac{1 - e^{-\frac{r_i T_s}{L_i}}}{r_i} \tag{3}$$

and,

$$\theta_{op} = \tan^{-1}\left(\frac{v^*_{\beta i}(k)}{v^*_{\alpha i}(k)}\right). \tag{4}$$

There exists 6 sectors in the 3L-NPC inverter space vector diagram as highlighted in Fig. 2. θ_{op} changes for 60° to choose next optimal sector ($\mathfrak{R}_g$) starting at sector I for $0° < \theta_{op} < 60°$.

D. PREDICTIVE MODEL

The grid voltages ($v_{\alpha g}$ and $v_{\beta g}$) and currents ($i_{\alpha g}$ and $i_{\beta g}$) are used to predict the grid currents as shown below:

$$\begin{bmatrix} i^p_{\alpha g}(k+1) \\ i^p_{\beta g}(k+1) \end{bmatrix} = \Phi \begin{bmatrix} i_{\alpha g}(k) \\ i_{\beta g}(k) \end{bmatrix} + \Gamma \left\{\begin{bmatrix} v^p_{\alpha i}(k) \\ v^p_{\beta i}(k) \end{bmatrix} - \begin{bmatrix} v_{\alpha g}(k) \\ v_{\beta g}(k) \end{bmatrix}\right\}. \tag{5}$$

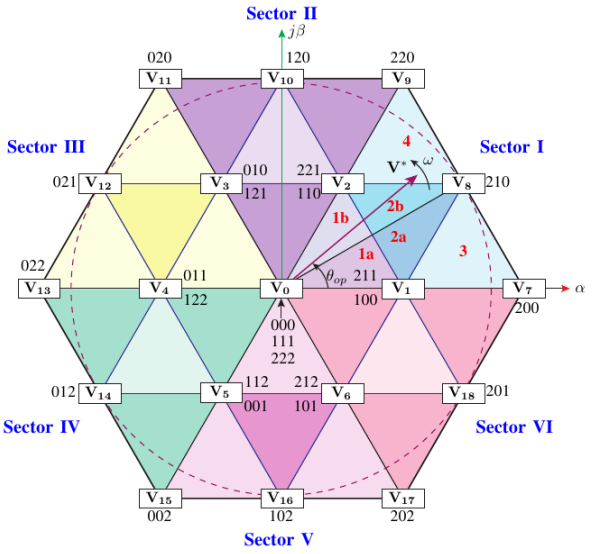

FIGURE 2. Space Vector Diagram of the 3L NPC inverter.

The model in (5) is then implemented again to further extend the predictions to the $(k+2)$ instant as:

$$\begin{bmatrix} i^p_{\alpha g}(k+2) \\ i^p_{\beta g}(k+2) \end{bmatrix} = \Phi \begin{bmatrix} i^p_{\alpha g}(k+1) \\ i^p_{\beta g}(k+1) \end{bmatrix} + \Gamma \left\{ \begin{bmatrix} v^p_{\alpha i}(k) \\ v^p_{\beta i}(k) \end{bmatrix} - \begin{bmatrix} v_{\alpha g}(k) \\ v_{\beta g}(k) \end{bmatrix} \right\}. \tag{6}$$

The output voltages of NPC inverter in (5) and (6) are predicted by using $\alpha\beta$-frame switching signals and measured DC-link capacitor voltages as demonstrated below:

$$\begin{bmatrix} v^p_{\alpha i}(k) \\ v^p_{\beta i}(k) \end{bmatrix} = v_{C1}(k) \begin{bmatrix} s_{\alpha 1}(k) \\ s_{\beta 1}(k) \end{bmatrix} + v_{C2}(k) \begin{bmatrix} s_{\alpha 2}(k) \\ s_{\beta 2}(k) \end{bmatrix} \tag{7}$$

where, $s_{\alpha 1}$, $s_{\alpha 2}$, $s_{\beta 1}$ and $s_{\beta 2}$ are the $\alpha\beta$-frame switching signals of the NPC inverter.

Future behavior of the DC-link capacitor voltages in the $(k+1)$ instant can be calculated as follows [25]:

$$\left.\begin{aligned} v^p_{C1}(k+1) &= v_{C1}(k) + \frac{T_s}{C_1} i_{C1}(k) \\ v^p_{C2}(k+1) &= v_{C2}(k) + \frac{T_s}{C_2} i_{C2}(k) \end{aligned}\right\} \tag{8}$$

where, C_1 and C_2 are the DC-link capacitors.

The model in (8) is further calculated for the $(k+2)$ instant as:

$$\left.\begin{aligned} v^p_{C1}(k+2) &= v^p_{C1}(k+1) + \frac{T_s}{C_1} i_{C1}(k), \\ v^p_{C2}(k+2) &= v^p_{C2}(k+1) + \frac{T_s}{C_2} i_{C2}(k). \end{aligned}\right\} \tag{9}$$

The DC-link capacitor currents i_{C1} and i_{C2} in (8) and (9) can be calculated as [26]:

$$\left.\begin{aligned} i_{C1} &= K_{a1}\, i_{ag} + K_{b1}\, i_{bg} + K_{c1}\, i_{cg} \\ i_{C2} &= K_{a2}\, i_{ag} + K_{b2}\, i_{bg} + K_{c2}\, i_{cg} \end{aligned}\right\} \tag{10}$$

where, the coefficients K_{x1} and K_{x2} are defined based on switching vectors as,

$$\left.\begin{aligned} K_{x1} &= \text{sgn}(1 - \mathbf{S_x}) \cdot \text{sgn}(\mathbf{S_x}) \\ K_{x2} &= \text{sgn}(0 - \mathbf{S_x}) \end{aligned}\right\} x \in \{a, b, c\} \tag{11}$$

where, $\mathbf{S_x}$ corresponds to the switching vectors of three phases. sgn(x) is the signum function that can be defined as demonstrated below:

$$\text{sgn}\,(x) = \begin{cases} -1 & \text{if } x < 0, \\ 0 & \text{if } x \equiv 0, \\ +1 & \text{if } x > 0. \end{cases} \tag{12}$$

E. INTERMEDIATE COST FUNCTION CALCULATION

The control objective of regulation of $\alpha\beta$-frame grid currents and neutral-point voltage control is defined by a $(k+2)$ cost function as shown below:

$$\left.\begin{aligned} g(k) = &\left[\widehat{i}^*_{\alpha g}(k+2) - i^p_{\alpha g}(k+2)\right]^2 \\ &+ \left[\widehat{i}^*_{\beta g}(k+2) - i^p_{\beta g}(k+2)\right]^2 \\ &+ \lambda_{dc}\left[v^p_{C1}(k+2) - v^p_{C2}(k+2)\right]^2. \end{aligned}\right\} \tag{13}$$

In (13), $\lambda_{dc} = I_{Bg}/v^*_{dc}$ is the weighting factor for neutral-point voltage control, where I_{Bg} is the base *rms* grid current.

The cost function values calculated in (13) are stored for the duty cycle calculations as opposed to classical PCC, where they are used to produce gating signals.

F. DUTY CYCLES CALCULATION

The duty cycles for three stationary voltage vectors are computed by trigonometric properties as follows:

$$\left.\begin{aligned} d_x &= \frac{g_y\, g_z}{g_x\, g_y + g_x\, g_z + g_y\, g_z}, \\ d_y &= \frac{g_x\, g_z}{g_x\, g_y + g_x\, g_z + g_y\, g_z}, \\ d_z &= \frac{g_x\, g_y}{g_x\, g_y + g_x\, g_z + g_y\, g_z}. \end{aligned}\right\} \tag{14}$$

The duty cycles in (14) yield that $d_x + d_y + d_z = 1$.

Using T_c as the period of the switching sequence's carrier waveform, the time durations for voltage vectors are calculated as,

$$T_x = d_x\, T_c,\ T_y = d_y\, T_c,\ T_z = d_z\, T_c, \tag{15}$$

where,

$$T_c = T_x + T_y + T_z. \tag{16}$$

G. OPTIMIZATION FUNCTION

A new optimization function is defined in terms of the duty cycles to calculate the average grid current error for each of the six triangular regions of an NPC inverter:

$$J(k) = d_x\, g_x + d_y\, g_y + d_z\, g_z. \tag{17}$$

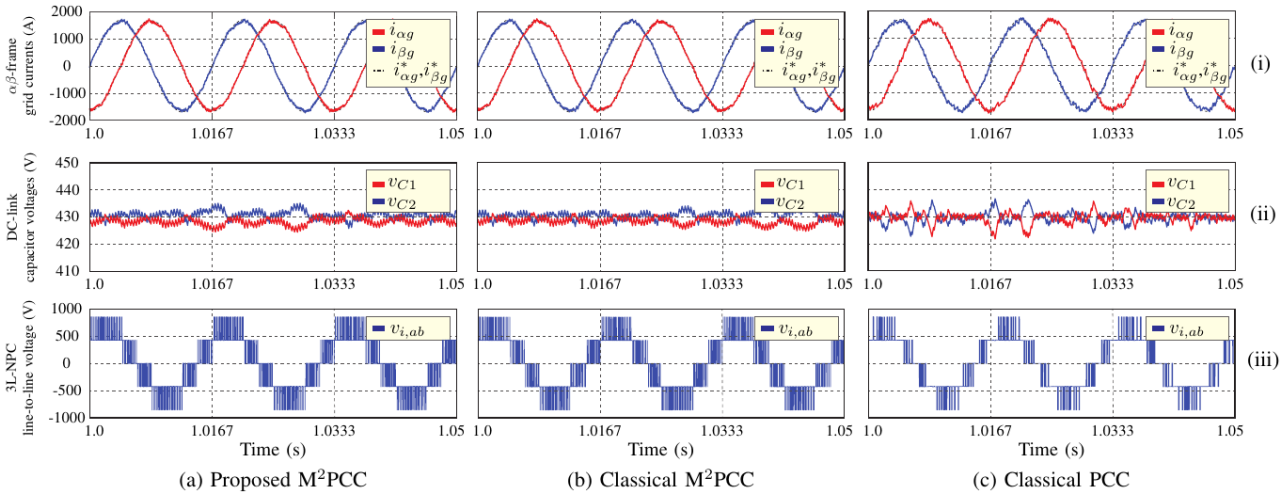

FIGURE 3. Simulated steady-state analysis of: (a) proposed M²PCC, (b) classical M²PCC, and (c) classical PCC methods at STC. (i) $\alpha\beta$-frame grid currents in A, (ii) measured DC-link capacitor voltages in V, (iii) 3L-NPC inverter line-to-line voltage in V.

The voltage vectors that minimize the optimization function in (17) are then used to implement a symmetrical switching sequence for the time durations established by T_x, T_y, T_z. This switching sequence follows the optimal vectors and completes the sequence for every interval of T_c.

III. SIMULATION RESULTS AND ANALYSIS

A. SIMULATION SETUP

The proposed M²PCC method is verified under steady-state and transient operating conditions with MATLAB/Simulink software. For this case, the Sunmodule plus SW 300 mono PV modules are implemented into the MATLAB/Simulink model. Details on the system parameters can be seen in Appendix– Table 2 [27]. To compensate for grid distortions in real-time, a grid voltage percentage total harmonic distortion (%THD) of 3.8% is measured from the experimental setup and inserted into the MATLAB/Simulink model.

B. STEADY-STATE ANALYSIS

The steady-state analysis of the PVES can be seen in Fig. 3, this analysis is accomplished under standard test conditions (STC), meaning solar irradiance $G_n = 1$ kW/m^2 and ambient temperature $T_n = 25°$ C, while assuming the grid reactive power Q_g^* as zero for unity power factor operation. Three separate control methods are accomplished and compared in Fig. 3: the proposed M²PCC, the classical M²PCC, and classical PCC. The sampling times for the M²PCC methods are set to $T_s = 200$ μs, and the sampling time for the PCC method is set to $T_s = 100$ μs. The difference in sampling times ensures that the average inverter switching frequencies are approximately equal, allowing for a more reasonable comparison of control methods. Fig. 3(i) shows the $\alpha\beta$-frame grid currents and the corresponding reference currents. The M²PCC methods exhibit better reference tracking and lower THD for grid currents than the classical PCC method. Fig. 3(ii) shows the balanced DC-link capacitor voltages for the proper functionality of the NPC inverter. Fig. 3(iii) is the NPC inverter line-to-line voltage containing five voltage levels.

C. HARMONIC ANALYSIS

Fig. 4 shows the FFT analysis of the proposed M²PCC method, the classical M²PCC method, and a classical PCC method at STC. The average inverter switching frequency ($f_{sw,inv}$) is held constant at 2500 Hz for the two M²PCC methods. The switching frequency is variable with the classical PCC method with an average value of 2641 Hz. The concentrated harmonics seen in Fig. 4(a) and Fig. 4(b) are generated from the constant switching frequency and are easier to filter than the variable switching frequency harmonics from the classical PCC in Fig. 4(c).

Table 1 provides further details regarding the $f_{sw,inv}$, the percentage tracking error of the grid currents ($\%e_{ig}$), the percentage THD ($\%\text{THD}_{ig}$), and the percentage neutral-point voltage balancing error ($\%e_{vdc}$). The M²PCC methods produce lower $\%\text{THD}_{ig}$ and $\%e_{ig}$ than the classical PCC method due to constant switching frequency operation. Also included in Table 1 is a set of results generated from a traditional VOC simulated model. The VOC results show the improved steady-state results that are expected when compared to the PCC. The proposed method produces similar steady-state response as classical M²PCC method despite the significant reduction in computational burden.

D. TRANSIENT ANALYSIS

To analyze performance under variable solar irradiance, G_n, a transient analysis is shown in Fig. 5 is accomplished. For this analysis, the ambient temperature T_n is constant at 25°C and the grid reactive power Q_g^* at zero for unity power factor. The initial solar irradiance G_n is 0.5 kW/m^2 and maintained there from $t = 0$ s to $t = 0.5$ s. From $t = 0.5$ s to 2.0 s, G_n is slowly ramped up to 1.0 kW/m^2 following a curved

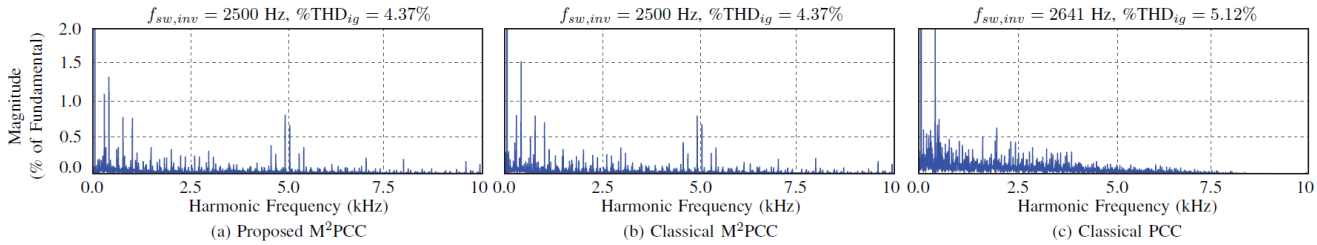

FIGURE 4. Simulated FFT analysis of: (a) proposed M^{2}PCC method, (b) classical M^{2}PCC method, and (c) classical PCC method at STC.

TABLE 1. Steady-state analysis of the PVES with proposed M^{2}PCC, classical M^{2}PCC, classical PCC, and classical VOC methods.

	Proposed M^{2}PCC (Simulated)	Classical M^{2}PCC (Simulated)	Classical PCC (Simulated)	Traditional VOC (Simulated)	Proposed M^{2}PCC (Experimental)	Classical M^{2}PCC (Experimental)	Classical PCC (Experimental)
Iterations	48	972	27	-	48	–	27
$f_{sw,inv}$	2500	2500	2641	2500	2500	–	2497
$\%e_{ig}$	4.37	4.37	5.12	4.47	5.71	–	6.13
$\%\text{THD}_{ig}$	3.15	3.15	4.83	4.56	5.42	–	5.92
$\%e_{vdc}$	0.34	0.34	0.27	0.3	0.64	–	0.26

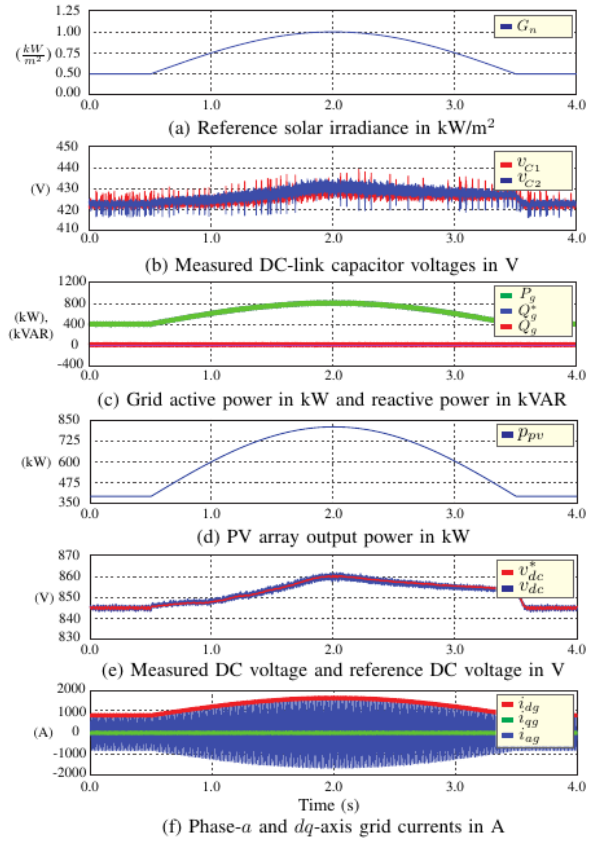

FIGURE 5. Simulated transient analysis of proposed M^{2}PCC method with programmed change in solar irradiance.

trajectory. From $t = 2.0$ s to 3.5 s, G_n is programmed to ramp down to 0.5 kW/m^2; this waveform is shown in Fig. 5(a). The magnitude of PV array power (p_{pv}) shown in Fig. 5(d), grid active power (P_g) shown in Fig. 5(c) and grid currents shown in Fig. 5(f) varies with respect to the irradiance G_n pattern. The DC capacitor voltages are balanced with less than ±1% error during entire transient period while staying close to the reference DC voltage (v^*_{dc}) seen in Fig. 5(b) and Fig. 5(e), respectively. The transient analysis presented here validates superior performance of proposed M^{2}PCC method during rapidly varying environmental conditions.

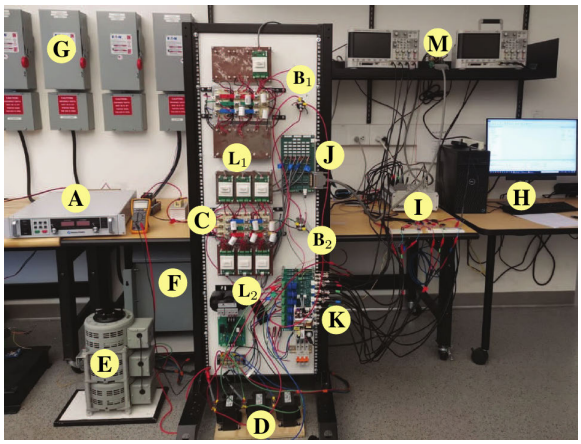

FIGURE 6. Experimental setup of proposed PVES with: (A) PV emulator, (B$_1$,B$_2$) DC-link capacitors, (C) 3L-NPC inverter, (D) grid harmonic filter, (E) Variac transformer, (F) isolation transformer, (G) 3-phase grid, (H) computer running ControlDesk, (I) dSPACE MicroLabBox, (J) interface board, (K) voltage and current sensors, (L$_1$,L$_2$) gate drivers, (M) oscilloscopes.

The analysis of both the steady-state and transient conditions for the proposed M^{2}PCC method shows comparable results with the classical M^{2}PCC method (with a reduction in computational burden) and superiority when compared to the classical PCC method.

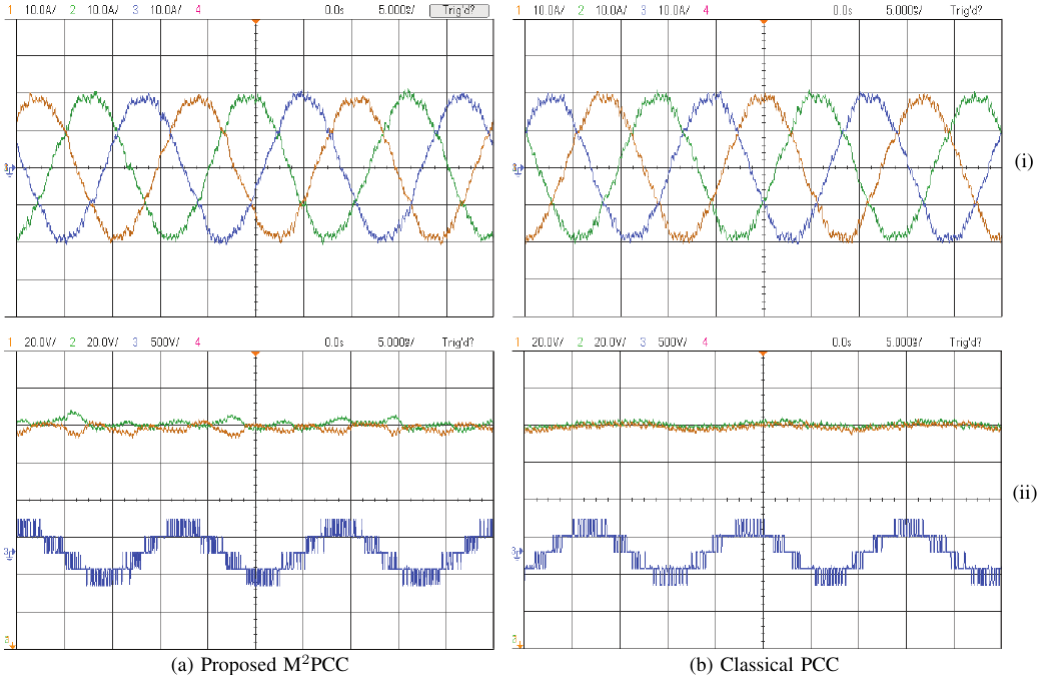

(a) Proposed M^{2}PCC (b) Classical PCC

FIGURE 7. Experimental results of PVES with: (a) proposed M^{2}PCC and (b) classical PCC. (i) Ch. 1, 2, 3: grid currents (i_{ag}, i_{bg}, and i_{cg}) in A (10A/div) and (ii) Ch. 1, 2: capacitor voltages (v_{C1}, v_{C2}) in V (20V/div), and Ch. 3: NPC inverter line-to-line voltage (v_{ab}) in V (500V/div).

IV. EXPERIMENTAL RESULTS

A. EXPERIMENTAL SETUP

To verify the proposed control method, a scale-down experimental setup has been developed using same per-unit values as in simulation studies for a more accurate comparison (see Appendix-Table 2). The experimental setup can be seen in in Fig. 6.A Magna-Power PV emulator running a photovoltaic power profile emulator program is used for a 5 kW PVES. The PV emulator is connected to DC-link capacitors and NPC inverter followed by a grid harmonic filter. The output is then connected to a Variac to establish a grid line-to-line voltage of 208 V, and lastly to an isolation transformer before grid injection. A dSPACE MicroLabBox is used to produce the real-time signals from a MATLAB/Simulink model to control the NPC inverter. The dSPACE MicroLabBox receives the measurements of currents and voltages and inserts them into the PCC and M^{2}PCC control methods and then sends the signals to an interface board to produce gating signals for the gate drivers.

B. STEADY-STATE ANALYSIS

The PV emulator is maintained under STC and a P&O MPPT algorithm is used to establish the maximum power capture. Experimental validation is not accomplished for the classical M^{2}PCC method due to issues with the high computational burden in the grid connected case. The experimental validation is accomplished with a switching frequency of 2500 Hz for the proposed M^{2}PCC and classical PCC methods. The proposed M^{2}PCC method preforms with the constant switching frequency of 2500 Hz while producing a grid current %THD$_{ig}$ of 5.42%. This is lower compared to the classical PCC method which produces a switching frequency of 2397 Hz and a grid current %THD$_{ig}$ of 5.92%. A summary of the measured values is shown in Table 1. The experimental results shown in Fig. 7 closely match the simulated results shown in Fig. 3.

The switching frequency in high power systems should remain low to reduce the switching losses. The THD is inversely proportional to the switching frequency, meaning that the lower switching frequency of 2500 Hz produces a THD of over 4%. Methods to reduce this would include increasing the size of the harmonic filter and increasing the switching frequency.

Fig. 7 demonstrates the steady-state performance of the proposed M^{2}PCC and classical PCC methods with the *abc*-frame grid currents (i_{ag}, i_{bg}, i_{cg}), DC-link capacitor voltages (v_{C1}, v_{C2}), and the inverter line-to-line voltage (v_{ab}). The plots in Fig. 7(i) demonstrates the grid currents in *abc*-frame while Fig. 7(ii) show the proper balancing of the DC-link capacitor voltages as well as the proper line-to-line voltage of the 3L-NPC inverter.

Fig. 8 show the robustness analysis with the percentage grid error (%e_{ig}) and the percentage THD (% THD) for both the proposed M^{2}PCC, classical PCC, and VOC simulated resulted, and PCC and M^{2}PCC experimental results with a change in the grid-side filter inductance. The system performances show that even with a change in the filter

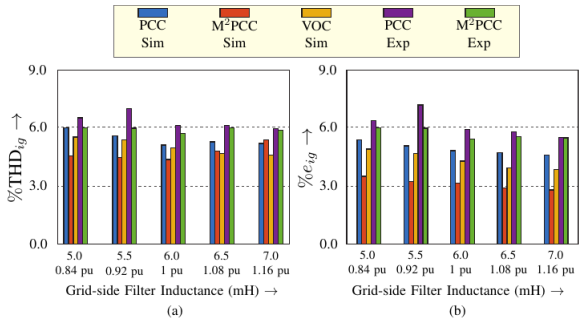

FIGURE 8. Performance of % THD $_{ig}$ and %e_{ig} with variations of grid-side filter inductance.

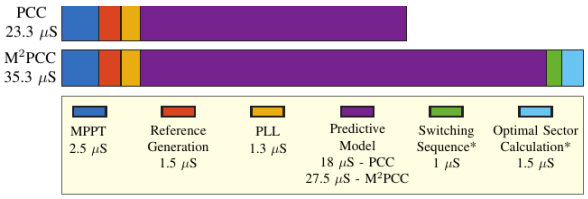

FIGURE 9. Execution times of the classical PCC and proposed M^{2}PCC methods, broken down into computation time of different steps in the process.

parameters, the proposed M^{2}PCC method is robust to the parameter changes and preforms better than the PCC and VOC methods.

Fig. 9 demonstrates the execution times of the proposed M^{2}PCC and classical PCC methods. It can be seen that of the two control methods, the MPPT, reference generation, and PLL are consistent across both the control methods. The PCC scheme requires 23.3 μs each instance, and the proposed M^{2}PCC scheme takes 35.3 μs, requiring an additional 12 μs. The predictive model of the M^{2}PCC method takes an additional 9.5 μs due to the objective function and triangular region calculations. The M^{2}PCC method also requires an additional 1 μs for the switching state and 1.5 μs for the optimal sector calculation. The computational requirement of 35.3 μs with the proposed M^{2}PCC method can easily be accommodated by the commercial digital control platforms available in the current market.

C. HARMONIC ANALYSIS

The constant switching frequency operation can be verified by the FFT accomplished for the proposed M^{2}PCC method in Fig. 10(a), where the peaks of the proposed M^{2}PCC method are centered around multiples of the constant switching frequency (2500 Hz). It can be shown in Fig. 10(b) that the classical PCC method produces a variable switching frequency that can be difficult to filter. The THD of grid currents is lower with the proposed M^{2}PCC method than the classical PCC method due to constant switching frequency operation.

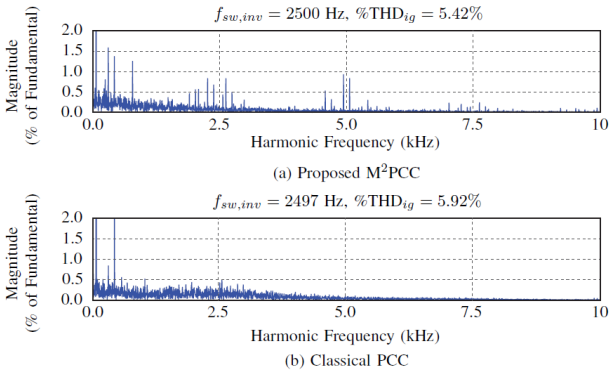

FIGURE 10. FFT analysis of experimental results for (a) proposed M^{2}PCC method, and (b) classical PCC method at STC.

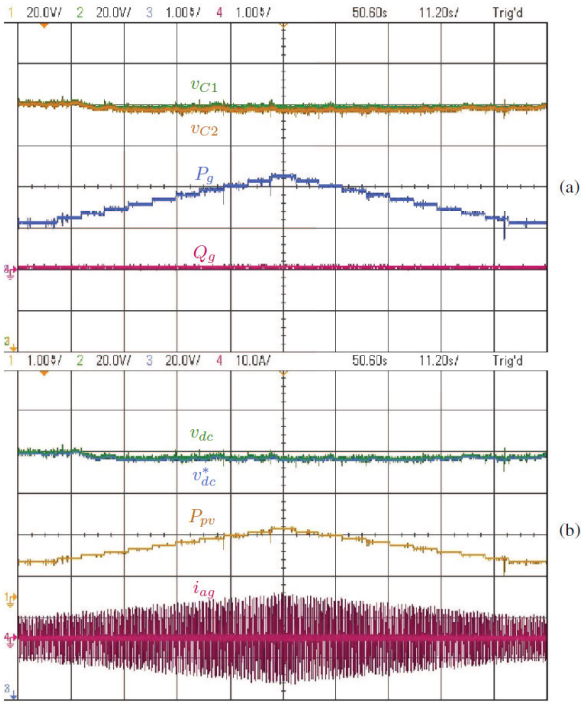

FIGURE 11. Transient analysis of proposed M^{2}PCC method with a low rise and fall in solar irradiance, where (a) Ch. 1, 2 are the DC-link capacitor voltages (v_{C1}, v_{C2}) in V (20V/div), Ch. 3, 4 are the grid active and reactive power (P_g, Q_g) in kW and kVAR respectively (1kW/div), (b) Ch 2, 3 is the DC-link voltage and DC-link reference voltage (V_{dc}, V^*_{DC}) in V (20V/div), Ch. 1 is the PV power in kW (1kW/div), and Ch. 4 is the phase-a grid current in A (10A/div).

D. TRANSIENT ANALYSIS

Results shown in Fig. 11 show the transient analysis of the proposed M^{2}PCC method with a programmed change in solar irradiance. The solar irradiance is programmed in the PV emulator to start at 0.5 kW/m^2 and increase at a rate of 0.05 kW/m^2 by 5 second intervals until it reaches rated (1 kW/m^2). Then the irradiance is programmed to follow the same pattern in reverse back down to 0.5 kW/m^2. These results show the systems capability in achieving superior

transient performance under rapid environmental changes, while remaining stable in a grid connected environment. Fig. 11(a) Ch. 3, 4 show the grid active and reactive power and Fig. 11(b) Ch. 1 shows the PV output power, both show a strong match with the change in solar irradiance programmed by the PV emulator. The grid phase-*a* current is seen in Fig. 11(b) Ch. 4 and demonstrates an increase and decrease in current that match the PV emulator. Fig. 11(a) Ch. 1, 2 show the DC-link capacitor voltages and Fig. 11(b) Ch. 2, 3 show the DC voltage and reference voltage, both show proper functionality of the PVES balancing the DC-link voltage and matching the DC reference voltage.

Fig. 12 demonstrates a programmed step change in the solar irradiance from 1.0 kW/m^2 to 0.5 kW/m^2. The plots in Fig. 12 are the grid phase-*a* current in Ch. 3, and Ch. 1 and 2 are the grid *dq*-axis currents. Due to the limitations of PV emulator, a slew rate of 100 mS is used for transition from 1.0 kW/m^2 to 0.5 kW/m^2. This demonstrates the system performance to a dramatic change in solar irradiance and the rapid transition in grid currents.

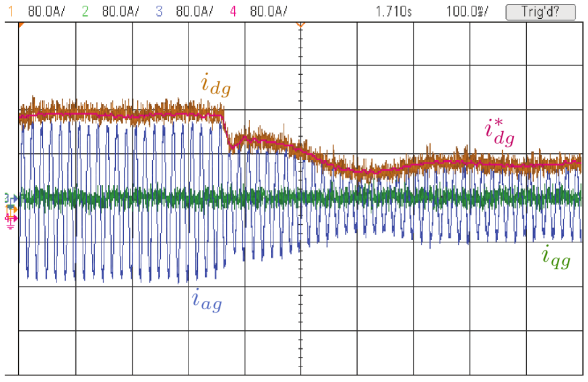

FIGURE 12. Experimental results of PVES with programmed step change in solar irradiance from 1.0 kW/m^2 to 0.5 kW/m^2.

V. CONCLUSION

A computationally efficient M^{2}PCC method is developed for a 3L-NPC inverter based PVES. The proposed M^{2}PCC method is validated using MATLAB simulations and dSPACE MicroLabBox based scaled-down experiments. The simulation and experimental results, which are in close match, demonstrated that the proposed method produces steady-state, transient and harmonic performance similar to the classical M^{2}PCC method, but with 95% reduction in computational burden. The proposed M^{2}PCC method exhibits superior performance than the classical PCC method during normal and perturbation conditions. The presented FFT plots confirm the constant switching frequency operation as highlighted by concentrated harmonics at multiples of the carrier frequency. The steady-state, transient and harmonic analysis presented for the proposed M^{2}PCC method demonstrates its readiness for deployment for commercial PV central inverters.

VI. FUTURE WORK

Future works on this topic include applying a fault-ride through method to follow grid codes or to explore the system response to allow for an unbalanced situation on the grid side. Additional experimentation comparing the proposed method to the VOC can also be completed.

APPENDIX

The values used in the simulated and experimental results are shown in Table 2.

TABLE 2. Parameters of the NPC inverter based PVES.

Description	Simulation SI Value	Experimental SI Value	p.u. Value
PV module V_{oc}	40.1 V	40.1 V	
PV module I_{sc}	10.23 A	10.23 A	
PV module V_{mpp}	31.6 V	31.6 V	
PV module I_{mpp}	9.57 A	9.57 A	
PV module P_{mpp}	302 W	302 W	
Number of series PV cells	60	60	
Series modules per string	27	14	
Parallel strings in array	100	1.18	
PV array V_{mpp}	853.2 V	442.4 V	
PV array I_{mpp}	957 A	11.3 A	
PV array P_{mpp}	817 W	4994 W	
Grid active power	817.3 kW	5 kW	1.0
Grid phase voltage	$400/\sqrt{3}$ V (rms)	$208/\sqrt{3}$ V (rms)	1.0
Grid frequency	60 Hz	60 Hz	1.0
Reference DC-link voltage	850 V	442 V	3.682
DC-link Capacitor	44.1 mF	1 mF	3.26
Grid-side filter inductance	0.13 mH	6 mH	0.25
Grid-side filter resistance	5.8 mΩ	325 mΩ	0.03
M^{2}PCC sampling time	200 μs	200 μs	
PCC sampling time	100 μs	100 μs	
Carrier wave period	400 μs	400 μs	
MPPT sampling time	5 ms	5 ms	
MPPT increment value	0.025 V	0.025 V	

REFERENCES

[1] S. Kouro, J. I. Leon, D. Vinnikov, and L. G. Franquelo, "Grid-connected photovoltaic systems: An overview of recent research and emerging PV converter technology," *IEEE Ind. Electron. Mag.*, vol. 9, no. 1, pp. 47–61, Mar. 2015.

[2] T. E. K. Zidane, A. S. Aziz, Y. Zahraoui, H. Kotb, K. M. AboRas, Kitmo, and Y. B. Jember, "Grid-connected solar PV power plants optimization: A review," *IEEE Access*, vol. 11, pp. 79588–79608, 2023.

[3] Y. Li, X. Yang, W. Chen, T. Liu, and F. Zhang, "Neutral-point voltage analysis and suppression for NPC three-level photovoltaic converter in LVRT operation under imbalanced grid faults with selective hybrid SVPWM strategy," *IEEE Trans. Power Electron.*, vol. 34, no. 2, pp. 1334–1355, Feb. 2019.

[4] S. Yan, C. Li, Y. Cui, X. Gao, and Y. Cai, "An improved FCS-MPC based on virtual vector expansion and sector optimization for 2L-VSCs," *IEEE Access*, vol. 10, pp. 127450–127460, 2022.

[5] S. Liu and C. Liu, "Virtual-vector-based robust predictive current control for dual three-phase PMSM," *IEEE Trans. Ind. Electron.*, vol. 68, no. 3, pp. 2048–2058, Mar. 2021.

[6] H. Wang, X. Wu, X. Zheng, and X. Yuan, "Model predictive current control of nine-phase open-end winding PMSMs with an online virtual vector synthesis strategy," *IEEE Trans. Ind. Electron.*, vol. 70, no. 3, pp. 2199–2208, Mar. 2023.

[7] S. A. Zaid, I. S. Mohamed, A. Bakeer, L. Liu, H. Albalawi, M. E. Tawfiq, and A. M. Kassem, "From MPC-based to end-to-end (E2E) learning-based control policy for grid-tied 3L-NPC transformerless inverter," *IEEE Access*, vol. 10, pp. 57309–57326, 2022.

[8] M. Aguirre, S. Kouro, C. A. Rojas, and S. Vazquez, "Enhanced switching frequency control in FCS-MPC for power converters," *IEEE Trans. Ind. Electron.*, vol. 68, no. 3, pp. 2470–2479, Mar. 2021.

[9] L. Tarisciotti, P. Zanchetta, A. Watson, J. C. Clare, M. Degano, and S. Bifaretti, "Modulated model predictive control for a three-phase active rectifier," *IEEE Trans. Ind. Appl.*, vol. 51, no. 2, pp. 1610–1620, Mar. 2015.

[10] J. Andino, P. Ayala, J. Llanos-Proaño, D. Naunay, W. Martinez, and D. Arcos-Aviles, "Constrained modulated model predictive control for a three-phase three-level voltage source inverter," *IEEE Access*, vol. 10, pp. 10673–10687, 2022.

[11] J. J. Silva, J. R. Espinoza, J. A. Rohten, E. S. Pulido, F. A. Villarroel, M. A. Torres, and M. A. Reyes, "MPC algorithm with reduced computational burden and fixed switching spectrum for a multilevel inverter in a photovoltaic system," *IEEE Access*, vol. 8, pp. 77405–77414, 2020.

[12] F. Donoso, A. Mora, R. Cárdenas, A. Angulo, D. Sáez, and M. Rivera, "Finite-set model-predictive control strategies for a 3L-NPC inverter operating with fixed switching frequency," *IEEE Trans. Ind. Electron.*, vol. 65, no. 5, pp. 3954–3965, May 2018.

[13] D. Zhou, C. Jiang, Z. Quan, and Y. R. Li, "Vector shifted model predictive power control of three-level neutral-point-clamped rectifiers," *IEEE Trans. Ind. Electron.*, vol. 67, no. 9, pp. 7157–7166, Sep. 2020.

[14] X. Liu, D. Wang, and Z. Peng, "A computationally efficient FCS-MPC method without weighting factors for NNPCs with optimal duty cycle control," *IEEE/ASME Trans. Mechatronics*, vol. 23, no. 5, pp. 2503–2514, Oct. 2018.

[15] Z. Zhang, C. M. Hackl, and R. Kennel, "Computationally efficient DMPC for three-level NPC back-to-back converters in wind turbine systems with PMSG," *IEEE Trans. Power Electron.*, vol. 32, no. 10, pp. 8018–8034, Oct. 2017.

[16] M. Easley, S. Jain, M. B. Shadmand, and H. Abu-Rub, "Computationally efficient distributed predictive controller for cascaded multilevel impedance source inverter with LVRT capability," *IEEE Access*, vol. 7, pp. 35731–35742, 2019.

[17] G. S. Kumar and R. Bhimasingu, "Optimal sector-based sequential model predictive control for current source rectifier," *IEEE J. Emerg. Sel. Topics Power Electron.*, vol. 10, no. 5, pp. 5833–5843, Oct. 2022.

[18] D. Xiao, K. S. Alam, M. Norambuena, M. F. Rahman, and J. Rodriguez, "Modified modulated model predictive control strategy for a grid-connected converter," *IEEE Trans. Ind. Electron.*, vol. 68, no. 1, pp. 575–585, Jan. 2021.

[19] A. Dahlmann, V. Yaramasu, S. Kouro, and M. Aguirre, "Computationally efficient predictive control of photovoltaic central NPC inverter with constant switching frequency," in *Proc. IEEE 7th Southern Power Electron. Conf. (SPEC)*, Nadi, Fiji, Dec. 2022, pp. 1–6.

[20] V. Yaramasu and B. Wu, *Model Predictive Control of Wind Energy Conversion Systems*. Hoboken, NJ, USA: Wiley, 2017.

[21] D. Zhu, X. Guo, B. Tang, J. Hu, X. Zou, and Y. Kang, "Feedforward frequency deviation control in PLL for fast inertial response of DFIG-based wind turbines," *IEEE Trans. Power Electron.*, vol. 39, no. 1, pp. 664–676, Jan. 2024.

[22] X. Guo, Y. Yang, and X. Zhang, "Advanced control of grid-connected current source converter under unbalanced grid voltage conditions," *IEEE Trans. Ind. Electron.*, vol. 65, no. 12, pp. 9225–9233, Dec. 2018.

[23] X. Lin, J. Yu, R. Yu, J. Zhang, Z. Yan, and H. Wen, "Improving small-signal stability of grid-connected inverter under weak grid by decoupling phase-lock loop and grid impedance," *IEEE Trans. Ind. Electron.*, vol. 69, no. 7, pp. 7040–7053, Jul. 2022.

[24] N. Femia, D. Granozio, G. Petrone, G. Spagnuolo, and M. Vitelli, "Predictive & adaptive MPPT perturb and observe method," *IEEE Trans. Aerosp. Electron. Syst.*, vol. 43, no. 3, pp. 934–950, Jul. 2007.

[25] E.-S. Jun, M. H. Nguyen, and S.-S. Kwak, "Model predictive control method with NP voltage balance by offset voltage injection for three-phase three-level NPC inverter," *IEEE Access*, vol. 8, pp. 172175–172195, 2020.

[26] M. Narimani, B. Wu, V. Yaramasu, Z. Cheng, and N. R. Zargari, "Finite control-set model predictive control (FCS-MPC) of nested neutral point-clamped (NNPC) converter," *IEEE Trans. Power Electron.*, vol. 30, no. 12, pp. 7262–7269, Dec. 2015.

[27] Solarworld. *Sunmodule Plus 285-300 Mono (5-Busbar) Solar Panel Data Sheet | SW-01-7510*. Accessed: Jul. 2022. [Online]. Available: https://www.solaris-shop.com/content/SW300%20Plus%20Mono%20Specs.pdf

ALEXANDER DAHLMANN (Member, IEEE) received the B.S. and M.S. degrees in electrical engineering from Northern Arizona University, Flagstaff, AZ, USA, in 2018 and 2020, respectively, where he is currently pursuing the Ph.D. degree in informatics.

His research interests include high-power converters, predictive control, multilevel inverters, and photovoltaic energy systems.

VENKATA YARAMASU (Senior Member, IEEE) received the Ph.D. degree in electrical engineering from Toronto Metropolitan University (formerly Ryerson University), Toronto, ON, Canada, in 2014.

From 2014 to 2015, he was as a Postdoctoral Research Fellow with Toronto Metropolitan University. In 2015, he joined Northern Arizona University, Flagstaff, AZ, USA, where he is currently an Associate Professor of electrical engineering with the School of Informatics, Computing, and Cyber Systems (SICCS). He has authored/co-authored more than 70 peer-reviewed articles, a book titled *Model Predictive Control of Wind Energy Conversion Systems* (Wiley–IEEE Press), eight book chapters, and 14 technical reports. His research interests include renewable energy, high-power converters, electric vehicles, and model predictive control.

Dr. Yaramasu was a recipient of more than 15 teaching and research excellent awards, including the Best Paper Award from *IET Electric Power Applications*, in 2020, and the Second Prize Paper Award from IEEE JOURNAL OF EMERGING AND SELECTED TOPICS IN POWER ELECTRONICS, in 2015.